ELSEVIER

Contents lists available at ScienceDirect

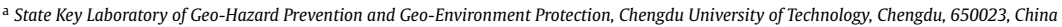
Earth and Planetary Science Letters

www.elsevier.com/locate/epsl



The intrinsic mobility of very dense grain flows

Wei Hu^a, Qiang Xu^{a,*}, Mauri McSaveney^{a,b}, Runqiu Huang^a, Yujie Wang^c, Ching S. Chang^d, Huaixiao Gou^a, Yangshuai Zheng^a



^b GNS Science, Lower Hutt, New Zealand

ARTICLE INFO

Article history:
Received 6 August 2021
Received in revised form 24 December 2021
Accepted 14 January 2022
Available online 31 January 2022
Editor: J.-P. Avouac

Dataset link: https://figshare.com/articles/ Intrisic mobility/11786190

Keywords: rock avalanche flash heating acoustic fluidization

ABSTRACT

High mobility of natural disasters with severe consequences is often reported in large landslides and in earthquake fault ruptures. The mechanism of high mobility keeps to be mysterious to date. In this study, we used high-speed rotary shear experiments under normal stress 1 MPa and with a rotary speed of 2 m/s on grains of four different minerals to show that the tested dry dense grain flows with crushable grains are highly mobile intrinsically. Granular flow quickly weakens to a very low viscosity (about 500 Pa.s), which is independent of grain composition. We find that when flow begins, grains are crushed to a special fractal structure in which most larger grain is surrounded by much smaller grains. This special structure provides a favourable condition for generating and propagating acoustic energy from the abrasion indicated by the scratches on the grains. The scratching generates very high frequency elastic energy (vibration) in the larger grains, which profoundly weakens all grain contacts so that the grain mass flows like a giant flood. Chatter-marked scratches made by smaller grains scouring across boulders in rock-avalanche deposits suggest that the same processes occur in nature. This finding is important for the explanation of the behaviour of dense grain flows at large strains and high strain rates.

© 2022 Elsevier B.V. All rights reserved.

1. Introduction

The puzzle of the unexpectedly high mobility of large geophysical flows has been reported as solved many times since Albert Heim drew attention to it after a disastrous landslide at Elm (Heim, 1882), Switzerland. Many hypotheses have been proposed to explain it in large rapid landslides: including mechanical fluidization (Heim, 1882: McSaveney, 1978), trapped-air fluidization (Kent, 1966), self-lubrication (Erismann, 1985), acoustic fluidization (Melosh, 1979, 1996); dynamic fragmentation (Davies and Mc-Saveney, 1999), and frictional heating (Vardoulakis, 2002; Goren and Aharonov, 2007). No consensus has emerged in more than a century, and debate has been raging on. Much the same may be said of the hypotheses for the surprisingly low frictional resistance in earthquake fault rupture (Tullis, 2015). In fault mechanics, researchers proposed mechanisms such as shear localization (Tullis, 2015), frictional melt lubrication (Sibson, 1975; Tsutsumi and Shimamoto, 1997; Hirose and Shimamoto, 2005; Di Toro et al., 2006), silica-gel lubrication (Goldsby and Tullis, 2002; Di Toro et al.,

2004), powder lubrication (Reches and Lockner, 2010), flash heating (Goldsby and Tullis, 2011), and thermal pressurisation (Han et al., 2007; Wibberley and Shimamoto, 2005; Rice, 2006). Here we use high-speed rotary shear experiments to show that dry dense grain flows with crushable grains are intrinsically highly mobile. They quickly weaken to an apparent viscosity like peanut butter, which is independent of grain composition. When flow begins, grains are crushed until every larger grain is surrounded by much smaller grains. As flow continues, the small grains scratch across larger-grain surfaces at high contact stresses. The scratching generates very high-frequency elastic energy (vibration) in the larger grains. The vibrations profoundly weaken all grain contacts so that the grain mass flows like a giant flood of peanut butter.

2. Materials and methods

A rotary-shear high-velocity friction apparatus for fault study is installed at the Institute of Geology, China Earthquake Administration (IGCEA) (Ma et al., 2014) (Fig. 1). The shear speed of this apparatus can be varied between 1.4×10^{-9} and 2.1 m/s and the maximum normal stress that can be applied is 80 MPa. We modified the specimen assembly of the original apparatus to hold thicker samples of granular materials to focus our experiments on





^c School of Physics and Astronomy, Shanghai Jiao Tong University, Shanghai, 200240, China

d Department of Civil Engineering, University of Massachusetts, Amherst, MA 01003, United States of America

^{*} Corresponding author.

E-mail address: xuqiang_68@126.com (Q. Xu).

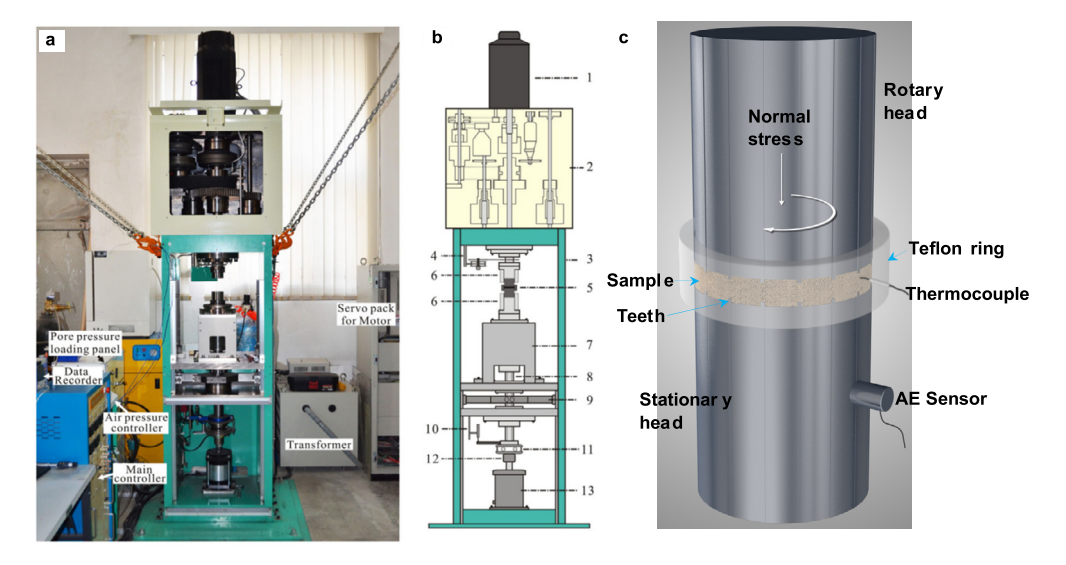


Fig. 1. Composition of the machine and sample. a. A photograph of the Rotary-shear Low to High-Velocity frictional testing machine (LHVR-Beijing). b. A schematic diagram of the main units of the apparatus. 1 servo-motor, 2 gear/belt system for speed change, 3 loading frame, 4 rotary encoder, 5 specimen assembly, 6 locking devices of specimens, 7 frame for holding the lower loading column, 8 axial loading column, 9 torque gauge, 10 axial displacement transducer, 11 thrust bearing, 12 axial force gauge, 13 air actuator. c. Details of sample and position of acoustic sensor and thermocouples. Its operation is illustrated in Movie S1.

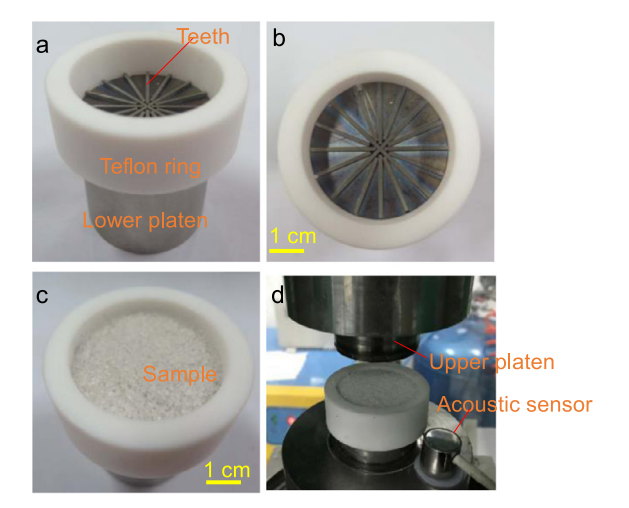


Fig. 2. Details of specimen assembly and position of acoustic sensor.

the grain flow. The new specimen assembly is shown in Fig. 1c and Fig. 2. We added teeth with heights of 1 mm on the lower and upper platens to prevent the grains from slipping at the interface with the platens, and increased the sample thickness from 1 mm (as described in Ma et al., 2014) to about 10 mm. The Titanium Alloy was used to make the head blocks as described by Yao et al. (2016). The assembly is shown in Fig. 1 and Fig. 2. Samples were constrained within \sim 40 mm diameter hollow Teflon cylinders (Fig. 1 and Fig. 2).

Our experiments sheared samples of granular materials of different hardness, at different normal stresses and different shear strain rates. These experiments were shear displacement-controlled tests by applying a known rotary shear speed. We sheared granulated quartz (Mohs hardness 7), dolomite (Mohs hardness 3.5-4), Feldspar (Mohs hardness 2.6-2.8), and corundum (Mohs hardness about 9.0). Quartz particles and corundum particles were industrial products. Dolomite particles and feldspar particles were crushed from the samples of Daguangbao landslides (Hu et al., 2019). We dried all the samples with room temperature (about 20 degrees) and room humidity (Relative Humidity (RH) about 39%) to be comparatively closer to the natural condi-

tion of granular sample. We did not dry the sample in the oven for 24 hours before testing, however, we knew the mechanical difference between the "room dry" particles and "oven-dry" sample (Sammis et al., 2011). The initial grain size of the materials was comparatively uniform from 0.85 mm to 1.18 mm. The individual grains of mass \sim 18 g sand samples for shearing were initially about 9 mm thick and were constrained within ~40 mm diameter hollow Teflon cylinders, with rotary shear imposed by a toothed steel platen which was used to prevent platen slip (Movie S1 and Fig. 1c and Fig. 2). Sample preparation for all the tests followed a quite similar procedure to achieve the same density state. We fixed the Teflon cell on the upper part of the Teflon cell (Fig. 1c). The compaction of the sample was divided into three layers, each about 3 mm thick with a given mass of particles, and we used a very small rammer to compact the sample. Before pouring the next layer of particles into the cell, we scratched the surface of the previous layer to avoid the artificial localization. A range of different normal loads (0.3-2 MPa) and shear speeds were applied in different experiments, with shear allowed to continue to very large strains. The acquisition frequency was 200 Hz for all experiments. The temperature of the sliding zone was monitored by a thermocouple mounted in the Teflon near the middle of the sample as shown in Fig. 1C. The details of measurement of temperature were described in supplementary information and shown in Fig. S1. The acoustic noise of each sample during shearing was monitored by acoustic sensors mounted on the non-rotating portion of the shear apparatus (Movie S1 and Fig. 1c). We used a wideband acoustic sensor (100-900 kHz) WD GB06 made by Physical Acoustic Corporation Mistras group. X-ray CAT Scans were carried out on a central column with diameter of 4 mm of quartz sample sheared dry at 1 MPa normal stress and rotary shear speed 2 m/s (corresponding to 230–400 /s strain rate) for \sim 25 m (see Fig. 9). A GE phoenix Nanotom S type 3D X-ray scanner was used to scan the internal structure of the ring shear sample after experiment. Scanning electron microscopy (SEM) was used to examine grain textures and surfaces at high magnification to resolve features smaller than 1 micron in size. The grain-size distribution of samples was measured by a laser particle analyser (Malvern Mastersizer 2000) by laser diffraction technology. The tested grain-size range was 0.01-3500 µm.

3. Test results

3.1. Calculation of friction and viscosity

Herein, we present new findings about dry dense flows of brittle grain materials, which shows that they all weaken profoundly with shear strain to reach an apparent viscosity of about 500 Pa.s, which is in the mid-range of values reported for peanut butter (Citerne et al., 2001). Moreover, that the weakening behaviour is independent of grain composition. Our study focused on the be-

- Friction coefficient

Sample thickness

haviour of large rock avalanches and experimental 40 mm diameter grain flows in a bespoke rotary shear apparatus under stresses and strain rates found in rock avalanches. We used the simple functions below to calculate the apparent coefficient of friction (μ) , the apparent viscosity (η) and shear strain rate $(\dot{\gamma})$:

$$\mu = \frac{\tau}{\sigma} \tag{1}$$

$$\eta = \frac{\tau}{\dot{\nu}} \tag{2}$$

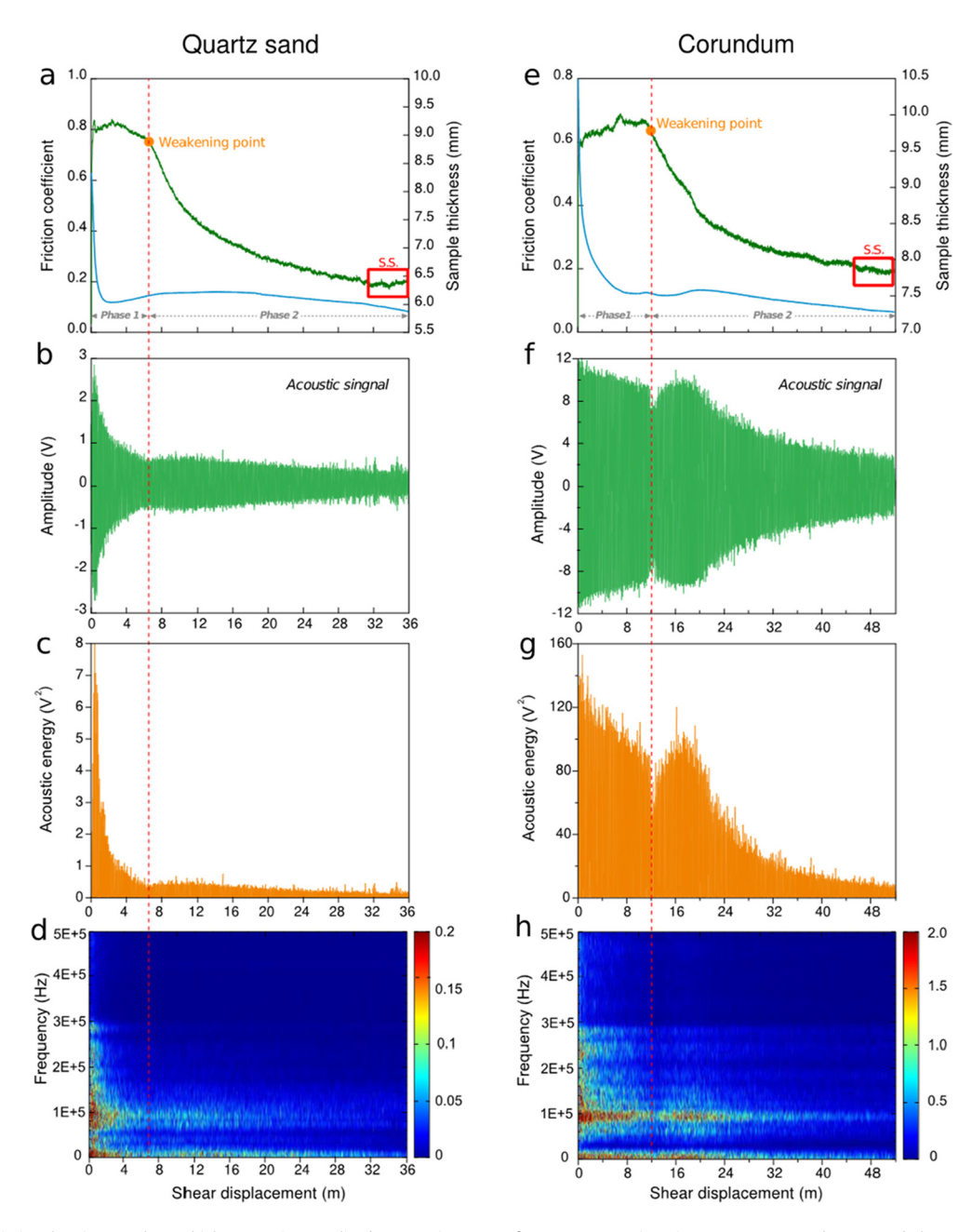


Fig. 3. Evolution of frictional resistance, layer thickness, noise amplitude, acoustic energy, frequency acoustic noise at 1 MPa normal stress and shear speed of 2 m/s or shear rates of 230–240 /s for various minerals: **a-d.** Quartz; **e-h.** Corundum; **i-l.** Feldspar and **m-p.** Dolomite; two phases of behaviour appear: an initial phase of high resistance and much noise, with strong contraction in thickness. This was followed by a small dilation until a threshold resistance was reached at a point coinciding with a local minimum in acoustic amplitude and acoustic energy. Samples then resumed contraction with slightly increased noise amplitude, and began a second phase of continual weakening until a steady state (s.s.) was reached after displacements which differed for each material (quartz, after ~36 m; corundum, ~40 m; dolomite, ~22 m; and feldspar, ~40 m).

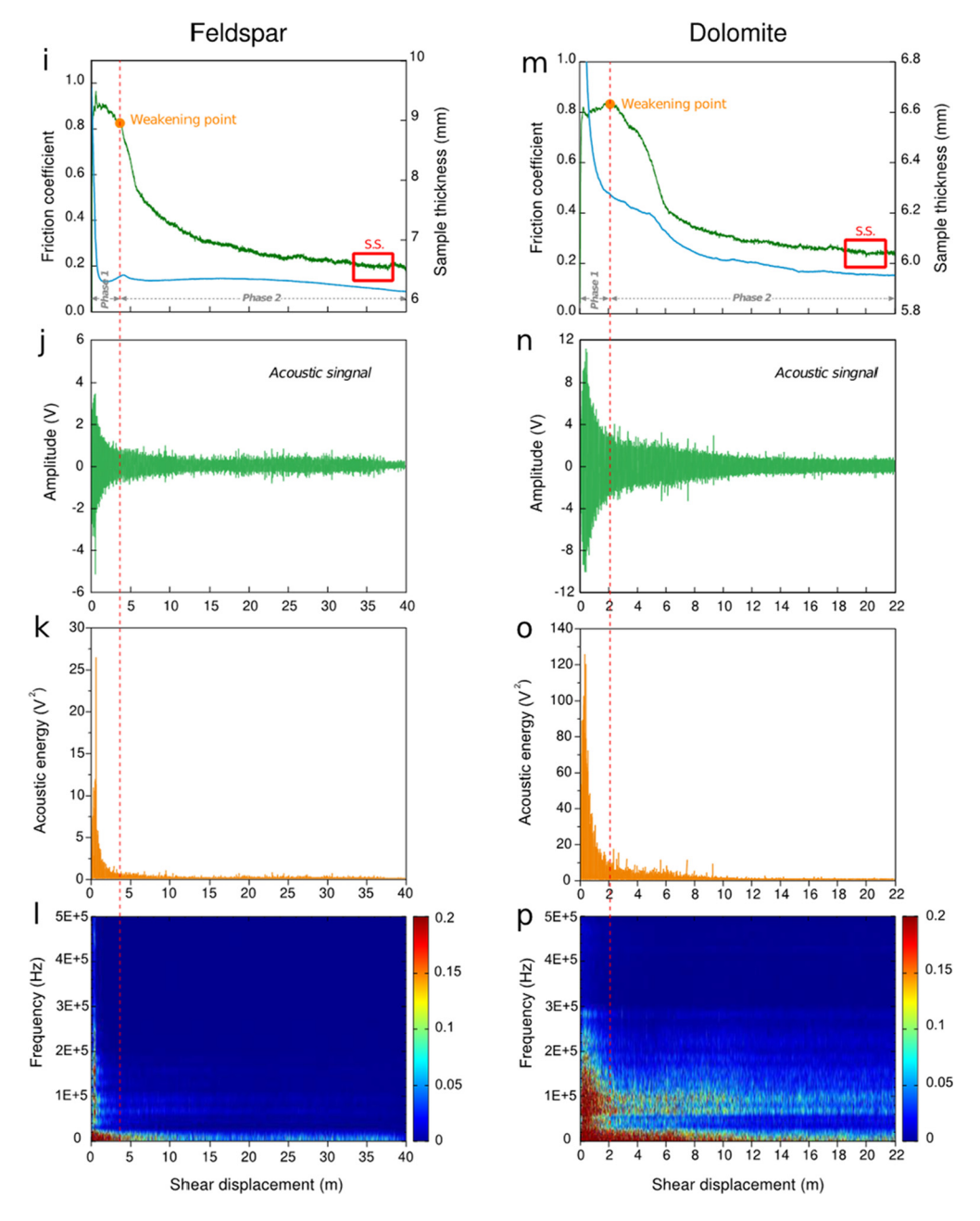


Fig. 3. (continued)

$$\dot{\gamma} = \frac{\partial u(y)}{\partial y} \tag{3}$$

where τ is shear stress (measured as shear resistance); σ is normal stress; u(y) is shear velocity average over horizontal cross-section, which represents the velocity profile along the thickness of the sample. $\dot{\gamma}$ is the shear strain rate. We followed a lot of previous work (Shimamoto and Tsutsumi, 1994; Hirose and Shimamoto, 2005; Di Toro et al., 2004) to make the assumption that the shear stress was a constant over the circular area. We used average values for shear velocity.

3.2. Mechanical and acoustic signals characteristics

Results from experiments at 1 MPa normal stress and a rotary speed of 2 m/s (corresponding to shear strain rate of approximately 230-400 /s) are shown in Fig. 3. Noise emitted during shearing was recorded by an acoustic sensor attached to the stationary platen (Movie S1 and Fig. 1c). We measured initial sample

thickness, and then monitored axial displacement as the sample was sheared, allowing sample thickness and average shear-strain rate to be calculated for the analysis of the experiments. In all experiments for different materials, the grain flows exhibited two phases of behaviour (Fig. 3). An initial phase of strong contraction of layer thickness (rapid axial strain) was accompanied by much noise. Thickness and noise amplitude decreased rapidly with shear displacement; both were due to an initial large amount of grain crushing (breakage). The contraction was followed by a small dilation of the shearing layer until a point was reached (weakening point) when profound weakening began, marking the beginning of a second phase of flow behaviour. Thereafter, the grain-flow frictional resistance decreased with increasing shear, but at a declining rate towards an apparent quasi-steady-state resistance. In phase 1, noise amplitude decreased rapidly with increasing shear strain and declining axial strain (Fig. 3). This indicated a decline in the rate of grain breakage. The weakening point marked a sudden decrease of shear resistance, but also coincided with a local minimum in noise amplitude. Early in phase 2, the noise amplitude increased to a smaller secondary peak, and then decreased gradually towards a steady state after much shear strain, but with little axial strain (change in layer thickness). Identical characteristics applied to all the different materials (Fig. 3), although the primary and secondary noise peaks varied between different materials, according to the relative hardness. Shear displacement to reach a given level of weakening also varied according to hardness. While it took more 10 m to strain weaken the hardest grains (corundum), it took only less than 2 m to strain weaken the softest grains (Feldspar).

One strategy to quantify and interpret the fluctuation behaviours of granular flow is characterizing a flow in terms of the granular temperature (Brilliantov and Pöschel, 2004; Ogawa, 1978). We followed the idea of Taylor and Brodsky (2017) to introduce the granular temperature into dense granular shear flow and consider acoustic energy as a proxy. We calculated acoustic energy based on our monitoring of acoustic noise and used the following equation:

$$E_a = \langle A_v^2 \rangle$$

where A_{ν} is the acoustic amplitude measured in volts. The results are shown in Fig. 3c, 3g, 3k, 3o. Acoustic energy followed very similar trend with the acoustic amplitude. In phase 1, the acoustic energy gradually decreased with shear displacement. The weakening point marked a sudden decrease of acoustic energy and coincided with a local minimum in noise amplitude. In phase 2, the acoustic energy first increased, and then gradually decreased until steady state was reached.

The acoustic signals were interpreted in the time domain through an empirical mode decomposition (EMD), combined with instantaneous frequencies determination (Hilbert–Huang transform). By the EMD technique, the signal is decomposed into a sum of oscillatory components (the intrinsic mode functions (IMFs)), each having a different frequency content, which can potentially highlight different material and process information. The IMFs shown in Fig. S2 are the intrinsic mode functions obtained through the Hilbert-Huang transform of the acoustic noise. The percentages on the right side indicate the relative power content of each IMF. The corresponding time-frequency spectrums are shown in Fig. 3d, 3h, 3i, 3p. The highest frequency obtained is about 5e+5 Hz.

The evolution of apparent friction coefficient with acoustic amplitude and temperature of three replicate grain-flow experiments is shown in Fig. 4. All the three tests were at a shear speed of 2 m/s and under normal stress of 1 MPa on quartz sands. As expected in any friction experiment, sample temperature increased during all experiments (Figs. 4a-c). The friction coefficient decreased as temperature increased (Fig. 4d). In all experiments, noise output experienced a rapid decrease of amplitude in Phase 1 as larger particles crushed. After the weakening point, the noise briefly experienced a small increase of amplitude with accumulating shear strain, and then slowly decreased to a steady-state level. The weakening point when the behaviour changed from Phase 1 to Phase 2 always corresponded to a local minimum in noise amplitude.

3.3. Evolution of grain size distribution of different shear displacement

We studied the evolution of the grain-size distribution, during 7 shear experiments on quartz sand under 1 MPa normal stress and with rotary speed of 1 m/s and 2 m/s, varying only the shear displacement (Fig. 5). Comparison of mechanical behaviours for these replicate experiments shows good repeatability (Fig. S4). The grain-size distributions with shear speed 1 m/s are shown in Fig. 5d. Four experiments (No. 1-4) with displacement

of 0.5, 1.0, 2.0 and 5.0 m were within the displacement range of Phase 1, and the other three (No. 5-7) with displacements of 10, 15 and 50 m were within Phase 2. Major weakening occurred after Point B (weakening point, see Fig. 5b), between the stopping points of experiments No. 3 and No. 5, at a shear displacement of about 7 m. There appeared also to be an earlier minor weakening (from point A to point B) at a slow rate, before the major weakening began. In the major weakening phase, the frictional resistance decreased, at a much higher but declining rate, until the sample friction coefficient reached a steady-state value. Point B (the weakening point) appeared to correspond to the lowest point in the acoustic-emission amplitude and acoustic energy (see Fig. 5c and 5d). Point C in Fig. 5b marked a transition from contraction to dilation of the deforming material and appeared to correspond to the moment of point A (initiation of the earlier gentle weakening). This transition from contraction to dilation can be explained by embedding and filling effect (Chang and Deng, 2017) (see Fig. S5). Before the weakening point (Fig. 5b), dilation appeared followed after a large sample contraction due to grain crushing. Why was there a comparatively small dilation? A "filling and embedding" effect may provide an explanation (Chang and Deng, 2017). In the initial shearing stage, small grains from crushed large grains filled into voids between large grains resulting in volume reduction. Continued grain breakage filled voids, and consequently, further breakage resulted in slower contraction or even created more voids. However, the volume-increase rate was much slower compared to the void-filling contraction. The breakage was reduced because stress concentrations around grain contact points became spread among many contacts with small grains (the coordination number of larger grains increases). Large grains became fewer and small grains became abundant as breakage continued. Small grains then pushed the large grains apart so that they became separate inclusions embedded in a small-grain matrix. The first scenario was the filling process and the second was the embedment process.

During Phase 1, the grain-size distribution changed greatly (Fig. 5e, samples 1-3) with many smaller grains formed from breakage of larger grains. When the grain flow entered Phase 2, the grain-size distribution appeared to have reached an "ultimate" state, after which the shape of the distribution changed very little, except for a gradual small increase in the proportion of finest grains. Very similar behaviour arose in experiments with quartz sand under a normal stress of 1 MPa and with rotary speed of 2 m/s (Fig. 5f-j). We followed the methods of Turcotte (1986), McDowell et al. (1996), Billi (2005), Dyer et al. (2012), Steacy and Sammis (1991), Sammis and Steacy (1995) to calculate the fractal dimension for samples after the tests.

$$N(L > d) = Ad^{-D}$$

where N is number of particles of size L greater than size d, D is the fractal dimension and A is a constant of proportionality. The calculation process of fractal dimension is shown in Fig. S6 and Fig. S7. As shown in Fig. 6a, the fractal dimension of our tests varies from 2.4 to about 2.9. The fractal dimension increases rapidly with the increase of shear strain before shear strain reaches about 1000%, and then become gradually stable. We also analysed the evolution of grain breakage index. We used the grain breakage index Br raised by Hardin (1985) as shown in Fig. 6b. We compared our results with the results of Coop et al. (2004). Coop et al. carried out ring shear tests on carbonate sand with rather low shear speed (1.9 mm/min). The comparison might indicate that the shear speed also plays an important role in the fragmentation process, and has a big influence on the fractal dimension of sample after shearing.

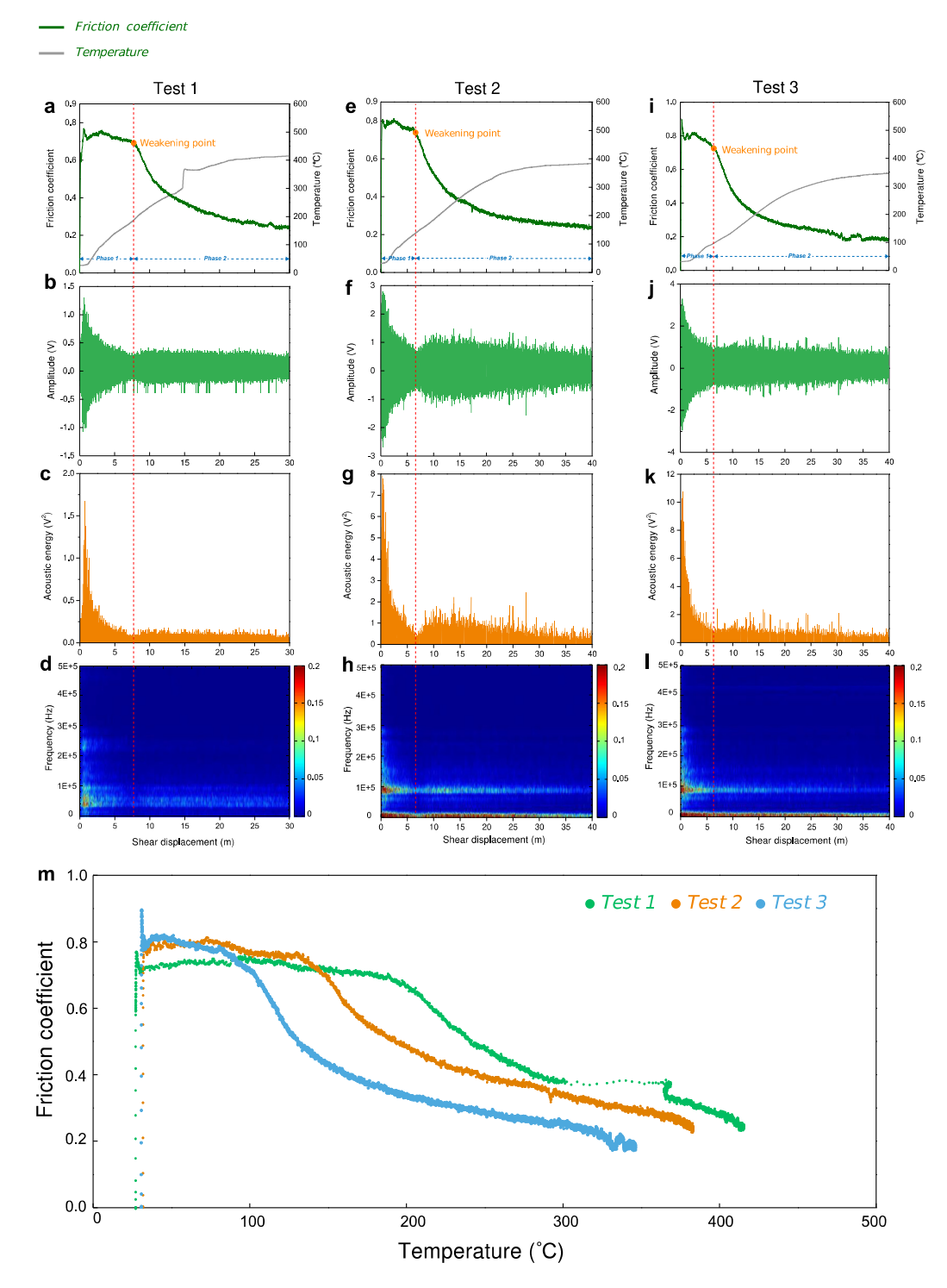


Fig. 4. Variation in apparent friction coefficient, noise amplitude, acoustic energy with shear-zone temperature during three replicate experiments for quartz sand under 1 MPa normal stress and a shear speed of 2 m/s or strain rate of 230-240 /s. **a-d.** Test 1; **e-h.** Test 2; **i-l.** Test 3; **e.** Apparent friction coefficient vs. sliding-zone temperature. In each experiment, noise amplitude rapidly decreased with increasing shear strain in Phase 1 as grains crushed less frequently. After a weakening point, acoustic amplitude gently increased and then slowly decreased to reach a steady state level after much shear strain. Weakening points corresponded to noise minima with no apparent association with temperature trend.

3.4. Fluid-like behaviour of tested dense granular flow

The viscosity and shear resistance of grain flows varied with shear displacement and shear strain rate (Fig. 7) for materials of different hardness under normal stress of 1 MPa and shear speed of 2 m/s. As shown in Fig. 7a, b, the viscosity quickly weakened to an apparent viscosity like peanut butter (about 500 Pa.s), which

was independent of grain composition. All flows exhibited two distinct phases of fluid-like behaviour. In phase 1 before the weakening point, as shown in Fig. 7c, for all the materials, the Phase-1 behaviour was a non-Newtonian like flow. In phase 2 after the weakening point, the shear stress decreased after the transition point with little change in shear strain rate, and the dense grain flows became much more fluid (much lower viscosity), tending

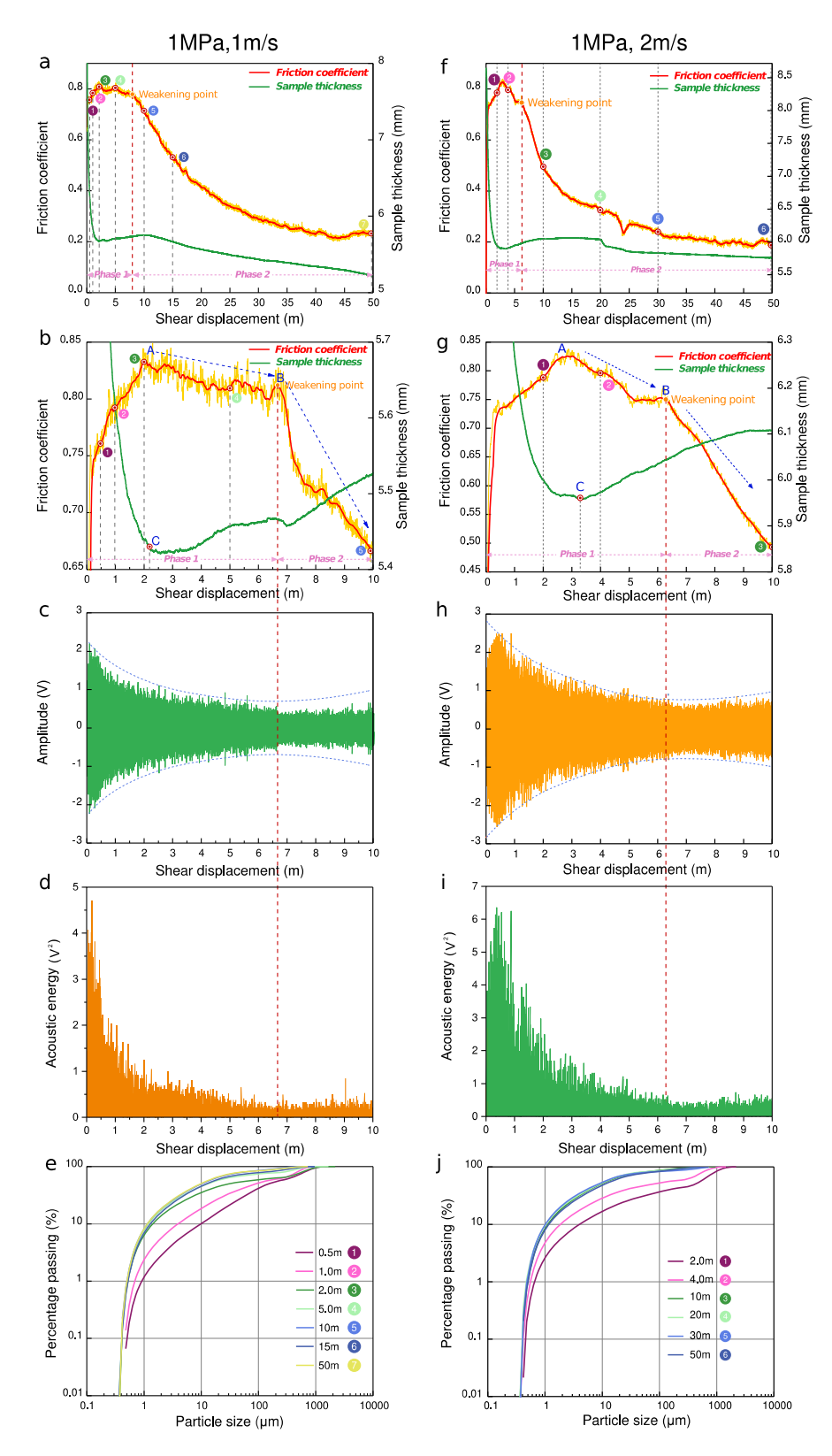


Fig. 5. Friction coefficient and thickness of quartz sand after different shearing distances at 1 MPa normal stress and respectively with rotary shear speed of 1 m/s and 2 m/s. **a-e.** Test results of samples at 1 MPa normal stress, with rotary shear speed of 1 m/s with different shear distances (respectively 0.5 m, 1.0 m, 2.0 m, 5.0 m, 10 m, 15 m, 50 m); **f-j.** Test results of samples at 1 MPa normal stress with rotary shear speed of 2 m/s with different shear distances, respectively 2 m, 4 m, 10 m, 20 m, 30 m, 50 m. **c and h.** Amplitude of acoustic noise; **d and i.** acoustic energy; **e and j.** grain-size distributions after different shear displacements. Circled numbers in **a and f.** mark end of each shear experiments. Size distributions (grading) rapidly become extremely wide-ranging and apparently fractal to sub-micron sizes. Grading shows an initial rapid change in **Phase 1** before strain weakening begins, and largely stabilizes thereafter in **Phase 2**. Point A in Fig. 5b marks initiation of minor weakening. Point B is initiation of major weakening (Weakening Point) and the lowest point in acoustic amplitude. After the weakening point is passed, finer particles continue to be fabricated by abrasion at the expense of a small reduction in proportion of larger grains. The rapid contraction in layer thickness changes at point C to slow dilation. By the beginning of Phase 2, finer grains dominate, with larger grains embedded among finer grains.

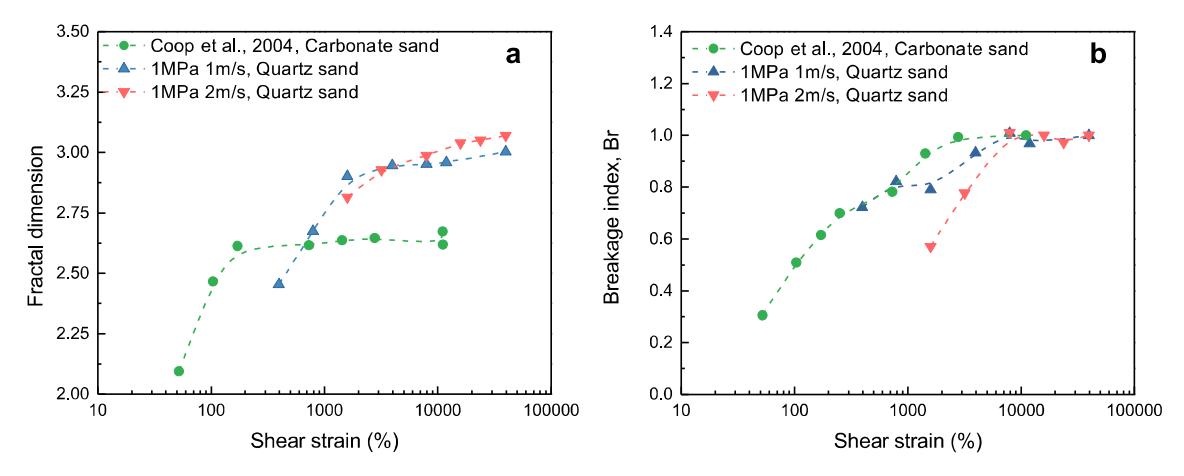


Fig. 6. The evolution of fractal dimension and breakage index with the increase of shear strain. a. Evolution of fractal dimension; b. Evolution of breakage index.

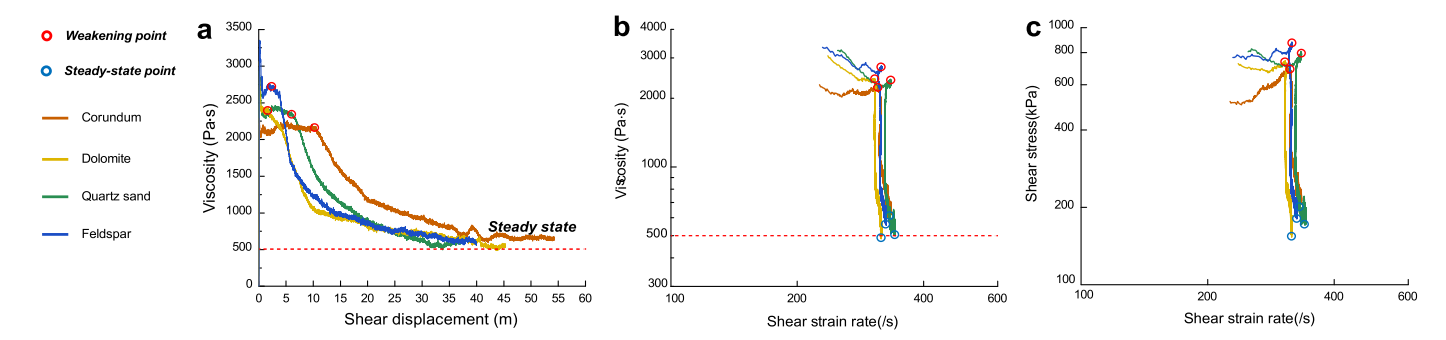


Fig. 7. Variation of viscosity or shear resistance with shear displacement or shear strain rate for four different brittle materials. a. Viscosity vs. shear displacement; b. viscosity vs. shear strain rate; c. shear resistance vs. shear strain rate. All materials behave as fluids, with two phases of behaviour. Phase 1 before the weakening point: all materials behave as a non-Newtonian flow; phase 2 after the weakening point: all show major weakening, in which grain flow becomes increasingly more fluid (lower shear resistance). The transition to the second phase of behaviour is abrupt. Shear resistance decreases with little change in strain rate and the dense grain flows become much more fluid (much lower shear resistance): a behaviour termed thixotropy (Mewis and Wagner, 2009; Skempton and Northey, 1952). Note that the viscosities of the phase 2 materials cannot be inferred from the gradients of these empirical curves.

toward an apparent steady state. This strain-weakening fluid behaviour is termed thixotropy in fluid and soil mechanics (Mewis and Wagner, 2009; Skempton and Northey, 1952).

3.5. Micro structure study and experimental, field evidence of stick-slip scratching

A typical sample of the quartz sand (Fig. 7) after rapid sliding with normal stress of 1 MPa and shear speed of 2 m/s was chosen for micro structure study. Due to the large compaction caused by extensive crushing during the rapid shearing, we obtained a whole block of sample after shearing. X-ray CAT Scans were carried out on central part (with diameter of 4 mm) of the sample for high resolution (Fig. 8). Larger grains were found to be highly angular, homogeneously distributed throughout the sheared mass and surrounded by smaller grains. Scanning electron microscope images (SEM) of a cross-section of the sample are shown in Fig. 9 at different scales. Almost all grains were highly angular, with larger grains always surrounded by much smaller grains (including nanoparticles). No larger grain was in contact with another large grain, and larger-grain contacts were only with clusters of much smaller grains.

SEM images of cross section of sample of quartz sand sheared dry at 1 MPa normal stress and 2 m/s for \sim 25 m are shown in Fig. 10. No localization was observed. At the end of shearing, the fractal distribution of grain sizes formed a specific packing structure, in which larger grains were completely embedded among smaller grains. Larger grains might experience only rare direct contacts with other larger grains during grain-mass deformation

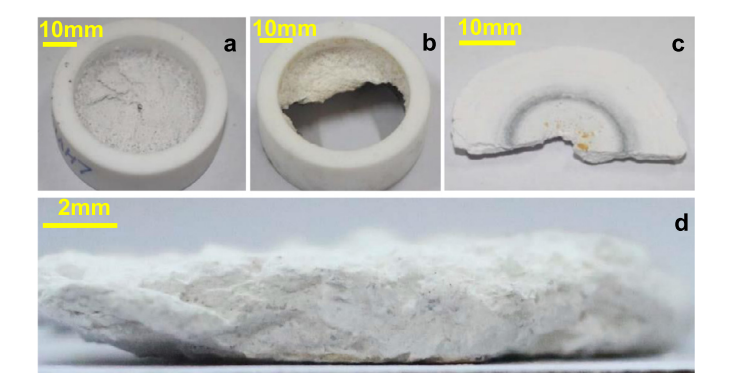


Fig. 8. The sample after rapid shearing. A typical sample of quartz sand after rapid shearing with normal stress of 1 MPa and shear speed of 2 m/s is presented. As shown in Fig. 3a, the sample experiences large contraction due to grain crushing at the beginning of the shearing. Due to this large contraction, we obtain comparatively complete sample after test for micro structure study. **a.b.c.** sample after the test; **d.** cross-section of the sample.

We separated some larger grains from sheared quartz-sand samples by rinsing them in water to wash away most fine grains. SEM images were taken of the surface textures of the larger grains, all of which were smaller than our initial finest starting size (0.85 mm). Grains with varying degrees of surface abrasion were found abundantly, while others were sharply angular. The scores on the surface of the grain shown in Fig. 11 might indicate other grains sliding along the grain's surface. In might be inferred that most fracture surfaces were crossed by tiny scratches (Fig. 11), which were caused by smaller grains sliding under high normal stress

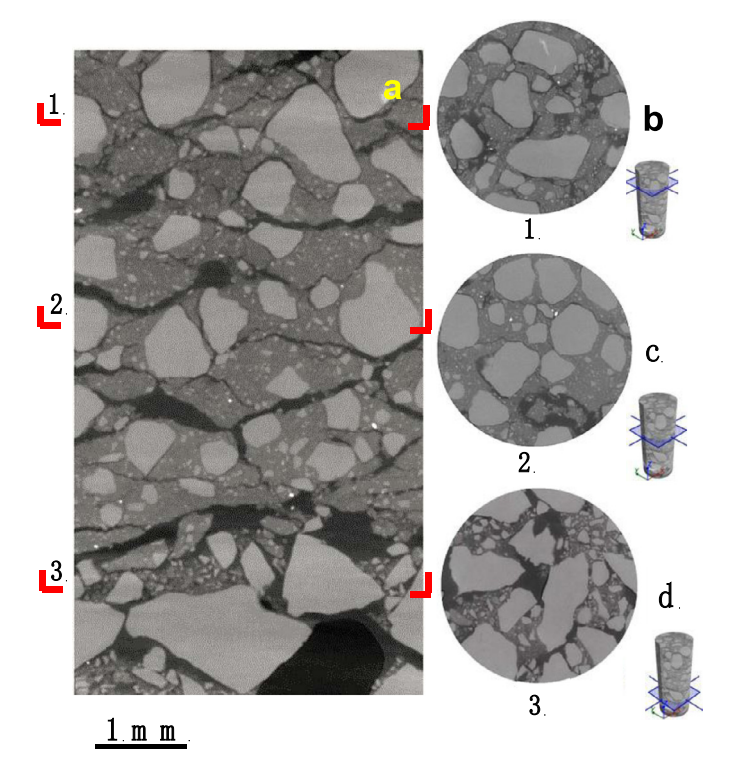


Fig. 9. X-ray CAT scans of sheared quartz sand. The sample was sheared at 2 m/s under a normal stress of 1 MPa. A central part of the sample (a column with diameter of \sim 4 mm) is chosen for the X-ray scan for much better resolution. **a.** Longitudinal section along the central axis; **b-d.** cross-sections at different depths in the sample. Highly angular grains are homogeneously distributed throughout the sheared mass, with larger grains always surrounded by much smaller ones (including nanoparticles). There is no evidence of shear localization. This image is similar to the cemented fault cataclasite shown by Heesakkers et al. (2011).

across the surfaces of the larger grain. Crossing scratches indicated differential relative motion of smaller grains across the surfaces of bigger grains which was likely to be caused by a combination of rotation of the larger grains due to the torque applied to them by shear strain gradients in the flow, and minor secondary circulation common to rotating fluid flows. Many larger-grain surfaces had multiple scratches caused by hard sub-micron sized grains of quartz (silica nanoparticles, Fig. 11e).

Some scratches had well developed chatter-marks (Fig. 11b and 11c). We guess that it is resulted from "stick-slip" frictional sliding. The pair scratches with regular chatter-mark spacing of about 30 nm (Fig. 11b and 11c) were gouged by a small grain sliding across the surface of the larger grain at high normal stress. We also found a larger-grain surface with few scratches (Fig. 11f), suggesting a relatively fresh fracture surface which had therefore collected few scratches.

Abundant scratches, many with chatter-marks, were also found at a much larger scale on boulders of the 2017 Xinmo rock avalanche (Fan et al., 2017) (boulder material: gneiss, Fig. 12), the 1991 Touzhai landslide (Xing et al., 2016) (basalt, Fig. 13). The triggering mechanisms of these two rock avalanches were different: the Xinmo landslide fell after creep deformation over years; the Touzhai rock avalanche fell seven days after heavy rain. The scratches were all caused by abrasion from smaller grains, and independent of triggering mechanism of rock avalanche.

4. Weakening mechanism

In the initial phase of shearing, all of our experimental dense grain flows behaved as relatively simple fluids across a wide range of shear strain rates (Fig. 6c) but then each reached a point when

their shear resistance weakened profoundly to a very low value with little change of shear strain rate. What could cause this major strain-weakening behaviour?

The weakening mechanism for large geophysical flows has been an important issue over the last several decades. Many hypermobility hypotheses have been formulated to explain rock avalanching and fault motion. For rock avalanches, mechanical fluidisation was first been proposed (Heim, 1882), followed by trapped-air fluidisation (Kent, 1966), self-lubrication (Erismann, 1985), acoustic fluidisation (Melosh, 1979), dynamic fragmentation (Davies and McSaveney, 2009) and frictional heating (Goren and Aharonov, 2007). In fault mechanics, researchers proposed mechanisms such as shear localization (Tullis, 2015), frictional melt lubrication (Sibson, 1975; Tsutsumi and Shimamoto, 1997; Hirose and Shimamoto, 2005; Di Toro et al., 2006), silica-gel lubrication (Goldsby and Tullis, 2002; Di Toro et al., 2004), powder lubrication (Reches and Lockner, 2010), flash heating (Goldsby and Tullis, 2011), and thermal pressurisation (Han et al., 2007; Wibberley and Shimamoto, 2005; Rice, 2006). After a careful study, we thought that flash heating and acoustic fluidization may be two principal mechanisms that cause sudden rheological weakening in the experiments of crushable materials.

4.1. Flash heating

Macroscopic weakening occurs due to thermal degradation of contact strength. At sufficiently high velocity, melting may occur. The process is often called 'flash' heating, after small 'stars of light' observed during sliding of transparent materials (Bowden et al., 1947). Flash heating has been proposed to be one of main mechanisms for weaker fault strength (Rice 1999, 2006, Goldsby and Tullis, 2011; Beeler and Tullis, 2003 Tsutsumi and Shimamoto, 1997; Di Toro et al., 2004; Han et al., 2007;). We believe that flash heating is one of the main mechanisms for the weakening in our tests. We monitored the sliding zone temperature and shear resistance during the rapid shearing. As shown in Fig. 4, we presented three repetitive tests on quartz sands with shear speed of 1 m/s and under normal stress of 1 MPa. When the temperature reached about 150 to 200 degrees, there was a dramatic weakening of friction coefficient in all the three repeated tests (Fig. 4d). These results support the hypotheses of flash heating.

One interesting point is that our observation of strong correlation between temperature rise and weakening (Fig. 4) seems to be in contrast to the analysis of Sammis et al. (2011), Reches and Lockner (2010), which showed strengthening of powder with rising temperature above 100 degrees due to evaporation of absorbed water of "room-dry" powder. In fact, we agree that the evaporation of absorbed water layer (about 20 nm thick, Sammis et al. (2011)) can increase the shear resistance of granular flow. However, in our tests, in the weakening regime, some other mechanisms of weakening, such as acoustic fluidization and flash heating, were more important than the evaporation of aborded water effect. So, we guess that evaporation of aborded water effect is hidden by other mechanisms in our tests.

4.2. Acoustic fluidization

Based on the test results, we believe that the acoustic fluidization also played an important role in the frictional weakening of our tests. Melosh (1979) proposed a new mechanism for reduction of shear resistance in a deforming granular aggregate, with possible relevance for impact crater collapses, landslides, and earthquakes. In this mechanism, termed acoustic fluidization, Melosh envisions that those acoustic waves reverberating inside the shearing aggregate could have sufficient intensity. Acoustic waves could exert large enough forces on the particles that they would be held

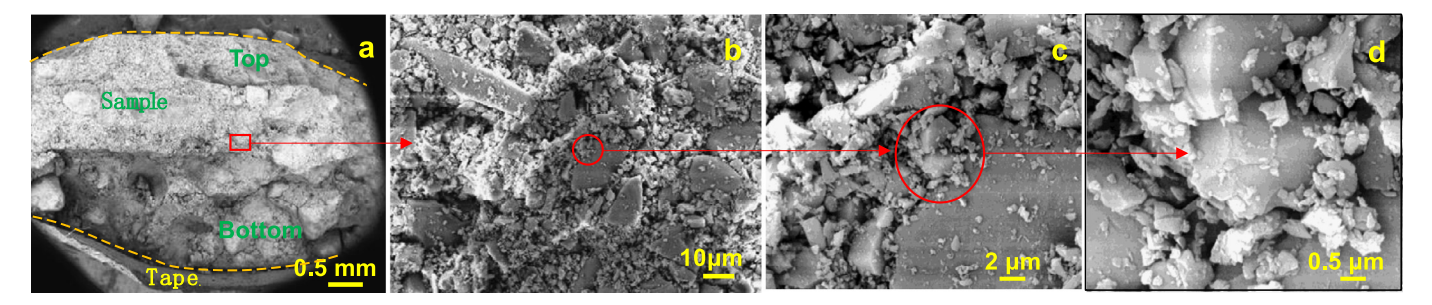


Fig. 10. SEM images of cross section of sample of quartz sand sheared dry at 1 MPa normal stress and 2 m/s for \sim 25 m. **a.** The structure of the cross section of the sample. **b-d.** Micro-structure of packing of the sample. Larger grains are found to be highly angular, homogeneously distributed throughout the sheared mass, and surrounded by smaller grains.

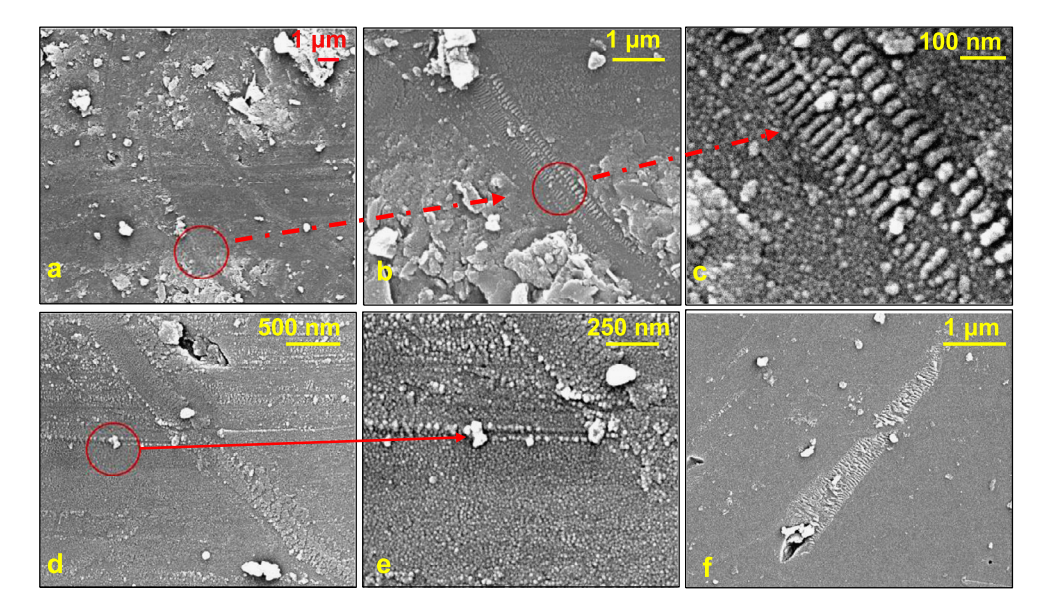


Fig. 11. Experimental evidence of stick-slip scratching. Smaller grains have scratched across the surface of a larger grain. In a, two scratch sets cross obliquely, suggesting that the bigger grain rotated during the flow. b and c, Tank-track-like scratches indicate stick-slip motion of a smaller grain across a grain surface. Chatter marks indicate that tiny grains have scoured larger grain surfaces, creating elastic body waves in the larger grain's rigid body (and surface waves on the larger-grain surface). These elastic strain waves reach and vibrate all its other grain contacts. d and e, a grain surface with fewer scratches, suggesting a relatively freshly broken surface (which therefore has collected fewer scratches).

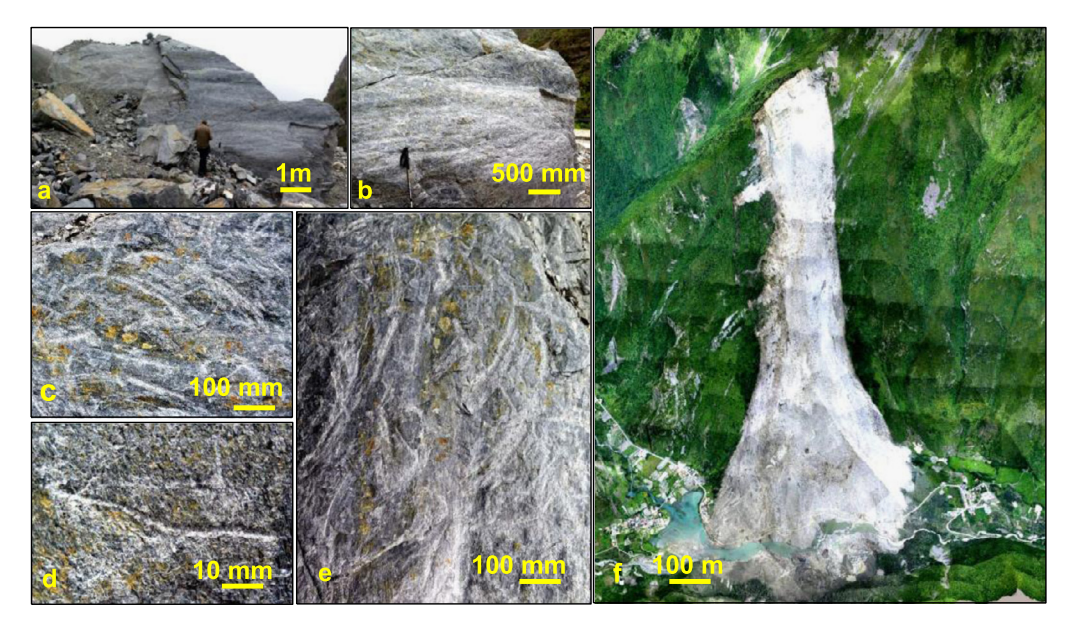


Fig. 12. Scratches on the boulder surfaces and composite UAV image of Xinmo landslide. a. and b. a boulder covered with curved scratches. c. scratches including a deep one; d. a polished and scratched surface of a boulder; e. curved scratches. f. UAV image of Xinmo landslide.

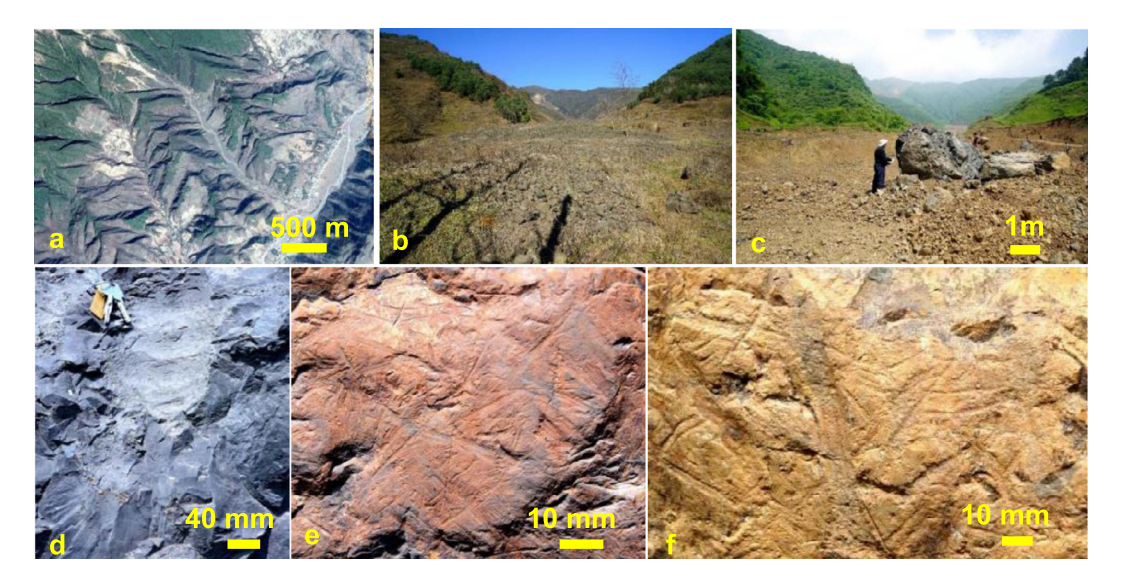


Fig. 13. Scratches on boulders and a satellite image (from Google earth) of Touzhai landslide: a. satellite image; b. and c. images of the landslide before and after excavation for construction fill; d. a giant scratch with three chatter marks on a weakly weathered basalt boulder; e. and f. scratches on strongly weathered boulders.

apart or would touch with less force. From our observation, we infer that extensive crushing induced specific packing and chatter marks induced elastic body wave may be important for the initiation of acoustic fluidization.

4.2.1. Special grain structure

At the initiation of shear in Phase 1 (Fig. 3 and Fig. 5a, 5b), extensive grain crushing (fragmentation) that occurred resulted in rapid volume reduction, with contraction of sample layer and release of much relatively large amplitude acoustic energy (Fig. 3 and Fig. 5c), but crushing was not associated with any weakening of the grain flow. Thus, it appears that several previously proposed explanations for the unusually fluid-like behaviour of such materials could be rejected as likely responsible for the hypermobility since they occurred in Phase 1 before the unusual behaviour was manifested (e.g. mechanical fluidization (Heim, 1882; McSaveney, 1978), and dynamic fragmentation (Davies and McSaveney, 1999)).

The absence of extensive weakening in phase 1 implies that a weakening mechanism was absent in phase 1, but it progressively developed during phase 2 (Fig. 3 and Fig. 5). During the phase-1 grain flows, the initial grain-size distributions changed rapidly towards apparent fractal distributions over most of their grainsize ranges, and reached at the weakening point (Fig. 5e). Strain weakening did not occur before the ultimate grain distribution was attained, although intensive grain breakage (fragmentation) had to have occurred to reach this size grading. An obvious inference from this is that fragmentation is not the weakening mechanism. The fractal distribution of grain sizes forms a specific packing structure, in which larger grains are completely embedded among smaller grains (Fig. 10) where they might experience only rare direct contacts with other larger grains during grain-mass deformation. The grain-crushing process (dynamic fragmentation) has increased the number of small grains in direct contact with the larger grains (increased the larger-grain co-ordination number) and thus inhibits further breakage of larger grains.

Larger grains were found to be highly angular, homogeneously distributed throughout the sheared mass and surrounded by smaller grains. Almost all grains were highly angular, with larger grains always surrounded by much smaller grains (including nanoparticles). No larger grain was in contact with another large grain, and larger-grain contacts were only with clusters of much smaller grains (Fig. 10b-d).

This specific structure emerged when the ultimate grain-size distribution had been achieved by grain crushing during the initial period of shear disturbance. This structural signature was absent in phase 1 but was present in phase 2 from the onset of weakening: it appeared to have been required for strain weakening to begin.

This special grain structure led to the phenomenon of strain weakening. As the structure was formed, strain weakening became apparent (strain weakening point) (Fig. 5). After the weakening point, the grain-size distribution changed very little (Fig. 5d), tending towards a fractal grain-size distribution. The small changes came from an increase in the amount of very fine grains (nanograins less than 1 micron across) resulted from grain breakage and attrition (abrasion). These nano-grains separated larger-sized grains, and this separation was associated with progressive decrease in shear resistance of the grain flow after the weakening point.

4.2.2. Elastic body wave-induced dense granular flow fluidization

The structure provided a favourable condition for generating and propagating acoustic energy from the abrasion indicated by the scratches on grains. The structure left many small grains surrounding each large grain in direct high-stress contact with the surfaces of the large grain. At this stage, further large-scale grainmass deformation was mostly frictional slip of very small grains against the surfaces of larger grains, with very little permanent deformation (breakage) of larger grains.

The chatter marks in Fig. 11 might indicate that the surfaces of larger grains were being scoured by hard nanoparticles, each creating dynamic elastic body waves in the rigid material of the larger grains (and surface waves on the larger grain surface). These elastic strain waves could be transmitted through the rigid elastic grain material to all the larger grains' other contacts with surrounding small grains. The regular spacing in the chatter-marks sets in Fig. 11c and 11f are 27 and 33 nm indicated vibration wavelengths of 27 and 33 nm. We had a rough estimation of the body-wave frequency in the scratched grain. The average travel speed of elastic wave in quartz is about from 5.70 km/s to about 6.25 km/s. So, we could very roughly estimate that the frequency was from 1.6¹¹ Hz to about 2.0¹¹ Hz (far outside the detection threshold of our acoustic sensors).

With each scratch, all contacts of a larger grain with its adjacent sub-micron particles would vibrate at such high frequency. With the combination of surface vibrations and their interference

harmonics, the local shear stress (τ_l) and local normal stress (σ_l) at each contact would change cyclically. Whenever their ratio exceeded the coefficient of sliding friction (μ) , grain slip occurred $(\tau_l/\sigma_l > \mu)$ is the conventional dry Mohr-Coulomb failure criterion, ignoring cohesion in the deforming grain flow). This was slip between grains which would not occur without the addition of bodywave energy from scratching slips occurring elsewhere around the larger grains. Such vibration-induced slip is termed acoustic fluidization (Melosh, 1979). We reasoned that acoustic fluidization was why different materials appear to exhibit the same flow resistance (Fig. 7), because the flow resistance depended on the same process, that of vibration, overcoming normal stress and reducing frictional resistance. Our hypothesis is illustrated at the grain-scale in the accompanying video supplements (Movie S2 and S3).

4.3. Shear localization

Shear localization has been considered to be an important phenomenon in materials (Walley, 2007) and an important mechanism for weakening in the shearing of granular materials (Kitajima et al., 2010; French et al., 2016; Boulton et al., 2017). However, it was very curious that we did not find the evidence of shear localization in our experiment. As shown in Fig. 8, 9, 10, highly angular grains were homogeneously distributed throughout the sheared mass, with larger grains always surrounded by smaller ones (including nanoparticles): larger grains were only in contact with much smaller grains. If present, the shear localization would have been visible as a band or bands of finer grains. The larger grains were entirely surrounded by angular smaller grains. A slice was also cut from a longitudinal section of this sample and submitted to SEM imaging (Fig. S8). Again, no evident shear localisation was found. The reason why we did not find localization in our experiments was not very clear. One of the possible reasons is the difference of the sample assembly between our experiments and the previous high speed friction tests. As described in Section Materials and Methods, to focus our experiments on the grain flow Fig. 1c and Fig. 2, we modified the specimen assembly of the original apparatus to hold thicker samples of granular materials We added teeth with heights of 1 mm on the lower and upper platens to prevent the grains from slipping at the interface with the platens, and increased the sample thickness from 1 mm to about 10 mm. The thickness of the most of the original samples in previous rotary tests on fault gouge was about 1 mm. The large change of sample thickness from 1 mm to 10 mm may change and interface behaviour experiment into a real granular flow experiment.

5. Conclusions

In our experimental dense grain flows, we postulate that the above mechanism operates at the sub-micron scale in the presence of embedded "macro-grains" being scoured by the embedding sub-micron grains (Chang and Deng, 2017). This may be a true physical and micro-manifestation of acoustic fluidization in our experimental grain flows, where the largest grains are initially about 1 mm in diameter. At a macro-scale, we find much larger scratches with chatter-marks on surfaces of boulder-sized grains in the field, which leads us to propose that the same acousticfluidization process may operate during the dense grain flows of real rock avalanches, where a similar fractal grain-size distribution embeds larger grains in a flowing "matrix" of embedding grains. This body-wave activated strength reduction appears as a significant predictable strain weakening (thixotropy), independent of grain material, pore fluid, but strongly dependent on shear-strain rate to reach a constant value of low shear resistance.

CRediT authorship contribution statement

Author contributions: W.H., Q.X. and M.M. wrote the paper. W.H., H.X.G., Y.S.Z. performed the experiments. W.H., M.M., R.Q.H., C.S.C. and Q.X. analysed the data.

Declaration of competing interest

The authors declare that they have no known competing financial interests or personal relationships that could have appeared to influence the work reported in this paper.

Data availability

All the original data used in this work can be retrieved from the data set available in the link: https://figshare.com/articles/Intrisic_mobility/11786190.

Acknowledgements

We want to thank Yao Lu for helping us do the high-speed experiments. We are supported by National Basic Research Program of China: basic research fund (42090051), National Basic Research Program of China: basic research fund (41790433); National Science Fund for Excellent Young Scholars, China, 41822702.

Appendix A. Supplementary material

Supplementary material related to this article can be found online at https://doi.org/10.1016/j.epsl.2022.117389.

References

Beeler, N., Tullis, T., 2003. Constitutive relationships for fault strength due to flash-heating. In: 2003 SCEC Annual Meeting Proceedings and Abstracts. Southern California Earthquake Center, Palm Springs, CA, p. 66.

Billi, A., 2005. Grain size distribution and thickness of breccia and gouge zones from thin (<1 m) strike-slip fault cores in limestone. J. Struct. Geol. 27 (10), 1823–1837.

Brilliantov, N.V., Pöschel, T., 2004. Kinetic Theory of Granular Gases. Oxford University Press, Oxford.

Boulton, C., Yao, L., Faulkner, D.R., Townend, J., Toy, V.G., Sutherland, R., Ma, S.L., Shimamoto, T., 2017. High-velocity frictional properties of Alpine Fault rocks: mechanical data, microstructural analysis, and implications for rupture propagation. J. Struct. Geol. 97, 71–92.

Bowden, F.P., Stone, M.A., Tudor, G.K., 1947. Hot spots on rubbing surfaces and the detonation of explosives by friction. Proc. R. Soc. Lond. Ser. A 188, 329–349.

Citerne, Guillaume P., Carreau, Pierre J., Moan, M., 2001. Rheological properties of peanut butter. Rheol. Acta 40, 86–96.

Chang, C.S., Deng, Y.B., 2017. A particle packing model for sand-silt mixtures with the effect of dual-skeleton. Granul. Matter 19, 80–85.

Coop, M.R., Sorensen, K.K., Freitas, T.B., Georgoutsos, G., 2004. Particle breakage during shearing of a carbonate sand. Géotechnique 54 (3), 157–163. https:// doi.org/10.1680/geot.2004.54.3.157.

Davies, T.R., McSaveney, M.J., 1999. Runout of dry granular avalanches. Can. Geotech. J. 36, 313–320.

Davies, T.R., McSaveney, M.J., 2009. The role of rock fragmentation in the motion of large landslides. Eng. Geol. 109 (1–2), 67–79.

Di Toro, G., Hirose, T., Nielsen, S., Pennacchioni, G., Shimamoto, T., 2006. Natural and experimental evidence of melt lubrication of faults during earthquakes. Science 311, 647–649.

Di Toro, G., Goldsby, D.L., Tullis, T.E., 2004. Friction falls towards zero in quartz rock as slip velocity approaches seismic rates. Nature 427, 436–439.

Dyer, H., Amitrano, D., Boullier, A.M., 2012. Scaling properties of fault rocks. J. Struct. Geol. 45, 125–136.

Erismann, T.H., 1985. Flowing, rolling, bouncing, sliding: synopsis of basic mechanisms. Acta Mech. 64, 101–110.

Fan, X.M., et al., 2017. Failure mechanism and kinematics of the deadly June 24th 2017 Xinmo landslide, Maoxian, Sichuan, China. Landslides 14, 2129–2146.

French, M.E., Zhu, W.L., Banker, J., 2016. Fault slip controlled by stress path and fluid pressurization rate. Geophys. Res. Lett. 43, 4330–4339.

Goldsby, D.L., Tullis, T.E., 2002. Low frictional strength of quartz rocks at sub seismic slip rates. Geophys. Res. Lett. 29, 25.

- Goldsby, D.L., Tullis, T.E., 2011. Flash heating leads to low frictional strength of crustal rocks at earthquake slip rates. Science 334, 216–218.
- Goren, L., Aharonov, E., 2007. Long runout landslides: the role of frictional heating and hydraulic diffusivity. Geophys. Res. Lett. 34.
- Han, R., Shimamoto, T., Hirose, T., Ree, J.-H., Ando, J., 2007. Ultra low friction of carbonate faults caused by thermal decomposition. Science 316, 878–881.
- Hardin, Bobby O., 1985. Crushing of soil particles. Journal of Geotechnical Engineering, 111 (10).
- Heesakkers, V., Murphy, S., Reches, Z., 2011. Earthquake rupture at focal depth, part I: structure and rupture of the Pretorius fault, Tau Tona mine, South Africa. Pure Appl. Geophys. 168 (12), 2395–2425.
- Heim, A., 1882. Der Bergsturz von Elm. Z. Dtsch. Geol. Ges. 34, 74-115.
- Hirose, T., Shimamoto, T., 2005. Growth of molten zone as a mechanism of slip weakening of simulated faults in gabbro during frictional melting. J. Geophys. Res. 110. B05202.
- Hu, W., Huang, R.Q., McSaveney, M., Yao, L., Xu, Q., Feng, M.S., Zhang, X.H., 2019. Superheated steam, hot CO2 and dynamic recrystallization from frictional heat jointly lubricated a giant landslide: field and experimental evidence. Earth Planet. Sci. Lett. 510, 85–93.
- Kent, P.E., 1966. The transport mechanism in catastrophic rock falls. J. Geol. 74, 79–83.
- Kitajima, H., Chester, J.S., Chester, F.M., Shimamoto, T., 2010. High-speed friction of disaggregated ultracataclasite in rotary shear: characterization of frictional heating, mechanical behavior, and microstructure evolution. J. Geophys. Res. 115, R08408
- Ma, S.L., Shimamoto, T., Yao, L., Togo, T., Kitajima, H., 2014. A rotary-shear low to high-elocity friction apparatus in Beijing to study rock friction at plate to seismic slip rates. Earthq. Sci. 27, 469–497.
- McSaveney, M.J., 1978. Sherman Glacier rock avalanche, Alaska, U.S.A.. In: Developments in Geotechnical Engineering, vol. 14 (part A), pp. 197–258.
- McDowell, G.R., Bolton, M.D., Robertson, D., 1996. The fractal crushing of granular materials. J. Mech. Phys. Solids 44 (12), 2079–2101.
- Melosh, H.J., 1979. Acoustic fluidization: a new geologic process? J. Geophys. Res. 84, 7513–7520.
- Melosh, H.J., 1996. Dynamical weakening of faults by acoustic fluidization. Nature 379, 601–606.
- Mewis, J., Wagner, N.J., 2009. Thixotropy. Adv. Colloid Interface Sci. 147–148, 214–227.
- Ogawa, S., 1978. Multi-temperature theory of granular materials. In: Proceedings of the US-Japan Seminar on Continuum-Mechanical and Statistical Approaches in the Mechanics of Granular Materials. Tokyo, pp. 208–217.

- Reches, Z., Lockner, D.A., 2010. Fault weakening and earthquake instability by powder lubrication. Nature 467. 452–455.
- Rice, J.R., 1999. Flash heating at asperity contacts and ratedependent friction. EOS Trans. Am. Geoph. Union 80, F681.
- Rice, J.R., 2006. Heating and weakening of faults during earthquake slip. J. Geophys. Res. 111, B05311.
- Sammis, C.G., Steacy, S.J., 1995. Fractal fragmentation in crustal shear zones. In: Fractals in the Earth Sciences. Springer, Boston, MA, pp. 179–204.
- Sammis, C.G., Lockner, D.A., Reches, Z.E., 2011. The role of adsorbed water on the friction of a layer of submicron particles. Pure Appl. Geophys. 168 (12), 2325–2334
- Sibson, R.H., 1975. Generation of pseudo-tachylyte by ancient seismic faulting. Geophys. J. R. Astron. Soc. 43, 775–794.
- Shimamoto, T., Tsutsumi, A., 1994. A new rotary-shear high-speed frictional testing machine: its basic design and scope of research. In Japanese with English abstract. J. Tecton. Res. Group Jpn. 39, 65–78.
- Skempton, A.W., Northey, R.D., 1952. The sensitivity of clays. Géotechnique 3, 30–53.Steacy, S.J., Sammis, C.G., 1991. An automaton for fractal patterns of fragmentation. Nature 353, 250–252.
- Taylor, S., Brodsky, E.E., 2017. Granular temperature measured experimentally in a shear flow by acoustic energy. Phys. Rev. E 96, 032913.
- Tsutsumi, A., Shimamoto, T., 1997. High-velocity frictional properties of gabbro. Geophys. Res. Lett. 24, 699–702.
- Tullis, T.E., 2015. Mechanisms for friction of rock at earthquake slip rates. In: Schubert, G. (Ed.), Treatise on Geophysics, 2nd ed. Elsevier, Oxford, pp. 139–159.
- Turcotte, D.L., 1986. Fractals and fragmentation, I. Geophys. Res. 91, 1921–1926.
- Vardoulakis, I., 2002. Dynamic thermo-poro-mechanical analysis of catastrophic landslides. Géotechnique 52, 157–171.
- Xing, A., et al., 2016. Investigation and dynamic analysis of a catastrophic rock avalanche on September 23, 1991, Zhaotong, Landslides 13, 1035–1047.
- Walley, S.M., 2007. Shear localization: a historical overview. Metall. Mater. Trans. A 38, 2629–2654.
- Wibberley, C.A.J., Shimamoto, T., 2005. Earthquake slip weakening and asperities explained by thermal pressurization. Nature 436, 689–692.
- Yao, L., Ma, S., Platt, J.D., Niemeijer, A.R., Shimamoto, T., 2016. The crucial role of temperature in high-velocity weakening of faults: experiments on gouge using host blocks with different thermal conductivities. Geology 44 (1), 63–66. https:// doi.org/10.1130/G37310.1.